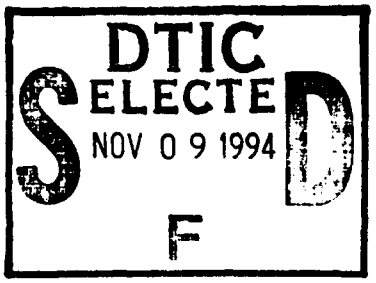

APPLICATION OF WAVELET-FILTERING TECHNIQUES TO INTERMITTENT TURBULENT AND WALL PRESSURE EVENTS.

PART I — EXPLORATORY RESULTS

Pablo B. Penafiel, Mario J. Casarella and Mark Kammeyer

The Catholic University of America

October 1994

APPLICATION OF WAVELET-FILTERING TECHNIQUES TO INTERMITTENT TURBULENT AND WALL PRESSURE EVENTS.

PART I — EXPLORATORY RESULTS

Pablo B. Penafiel, Mario J. Casarella and Mark Kammeyer

The Catholic University of America

October 1994

REPORT DOCUMENTATION PAGE

Form Approved
OMB No. 0704-0188

1. AGENCY USE ONLY (Leave Blank)	2. REPORT DATE	3. REPORT TYPE AND DATES COVERED
	October 25, 1994	Progress: Oct/1993 - Oct/1994

4. TITLE AND SUBTITLE
Application of Wavelet-filtering Techniques to Intermittent and Wall-pressure Events.

5. FUNDING NUMBERS
N00014-88-K-0141

6. AUTHOR(S)
Pablo B. Penafiel, Mario J. Casarella and Mark Kammeyer

7. PERFORMING ORGANIZATION NAME(S) AND ADDRESS(ES)
The Catholic University of America
Department of Mechanical Engineering
Washington D.C. 20064

8. PERFORMING ORGANIZATION REPORT NUMBER

9. SPONSORING/MONITORING AGENCY NAME(S) AND ADDRESS(ES)
Office of Naval Research
800 North Quincy St.
Alexandria, VA 22217-5000

10. SPONSORING/MONITORING AGENCY REPORT NUMBER

11. SUPPLEMENTARY NOTES

12a. DISTRIBUTION/AVAILABILITY STATEMENT
Approved for public release; distribution is unlimited.

12b. DISTRIBUTION CODE

13. ABSTRACT (Maximum 200 words)

Abstract

Large amplitude wall-pressure events, observed beneath a turbulent boundary layer, appear to be the signatures of intermittent organized motions within the turbulent flow. The temporal localization of these events could be applied to the active control of turbulent wall flows. This report presents preliminary results on utilizing time-frequency localization techniques (wavelet transforms) for the detection of these events. The advantage of these methods is that they do not require *a priori* assumptions regarding the features of the signal. A tutorial overview of these techniques is first presented. This is followed by a discussion of some exploratory results obtained from the application of wavelet filtering to wall pressure and turbulent temporal records acquired from wind tunnel experiments.

14. SUBJECT TERMS
wavelet filtering, wall-pressure fluctuations, turbulence
time-frequency localization, conditional sampling

15. NUMBER OF PAGES
42

16. PRICE CODE

17. SECURITY CLASSIFICATION OF REPORT	18. SECURITY CLASSIFICATION OF THIS PAGE	19. SECURITY CLASSIFICATION OF ABSTRACT	20. LIMITATION OF ABSTRACT
UNCLASSIFIED	UNCLASSIFIED	UNCLASSIFIED	

NSN 7540-01-280-5500

Standard Form 298 (Rev 2-89)
Prescribed by ANSI Std Z39-18
298-102

Contents

Abstract

Large amplitude wall-pressure events, observed beneath a turbulent boundary layer, appear to be the signatures of intermittent organized motions within the turbulent flow. The temporal localization of these events could be applied to the active control of turbulent wall flows. This report presents preliminary results on utilizing time-frequency localization techniques (wavelet transforms) for the detection of these events. The advantage of these methods is that they do not require *a priori* assumptions regarding the features of the signal. A tutorial overview of these techniques is first presented. This is followed by a discussion of some exploratory results obtained from the application of wavelet filtering to wall pressure and turbulent temporal records acquired from wind tunnel experiments.

Chapter 1

INTRODUCTION

1.1 Background

It has been widely postulated that large amplitude wall-pressure events can be used as a non-intrusive observation of the passage of organized flow structures. These organized motions are proposed to be the primary mechanism for the production of turbulence (cf. [1]). It is speculated that the temporal localization of these surface events could be used for the active control of turbulent wall flows.

The pressure fluctuations beneath a turbulent boundary layer are the integral effects of active (turbulent producing) and passive (high kinetic energy) flow structures throughout the boundary layer. It is the active structures that are of primary interest in a control system. Therefore, signal detection techniques on the temporal records of the pressure are required to discriminate between the two contributions. In the context of this paper, the pressure fluctuations of the passive motions will be considered as noise contamination on the pressure signatures of the active motions.

Previous work by Farabee and Casarella (cf. [2]) had shown that turbulent sources of the wall pressure spectrum can be attributed to flow activities at distinct locations across the boundary layer. They concluded that the inner layer is characterized by high frequency turbulent motions while the outer layer is characterized by low frequency structures. It is widely believed that the near-wall (active) structures can spatially extend to the overlap region and are thus not limited to a distinct spatial location. Clearly, conventional

frequency filtering techniques cannot be applied.

A more tractable approach is to examine the intermittent large-amplitude pressure events at the wall. These appear to be the footprint of the bursting process associated with the near-wall turbulent production mechanism (cf. [3]). Extensive work has been done using a range of schemes for the simultaneous detection of intermittent large-amplitude turbulent and wall-pressure events (cf. [4, 5]). Conditional sampling techniques are often used and these include detection algorithms based on:

- VITA on u with slope criteria
- VITA on u+LEVEL (cf. [6])
- Q2 and Q4 quadrant
- Peak pressure events

By averaging the collection of detected events, a correlation can be observed between turbulent events and peak pressure events. The number of events detected, and thus averaging, are affected by filtering techniques and various refinements to the detection algorithm. Furthermore, the shape of the detected events, including non-symmetric patterns, is strongly dependent on the alignment procedure used for averaging. It appears that an unbiased detection algorithm is required. This was the motivation for this investigation.

1.2 Review of Temporal Records

It is necessary to first examine the characteristic features of the temporal records of both, the fluctuating velocities within the flow, and simultaneous wall pressure. The data acquisition and conditioning, spectral content, and cross-correlation will be presented.

The experimental setup for the measurement of the time records used in the present study included pressure and velocity sensors. Two components of the velocity (streamwise and wall normal) were measured using a cross-wire anemometer. Simultaneous with the velocity measurements, the wall pressure fluctuations were recorded using a 1/8" B&K microphone with a

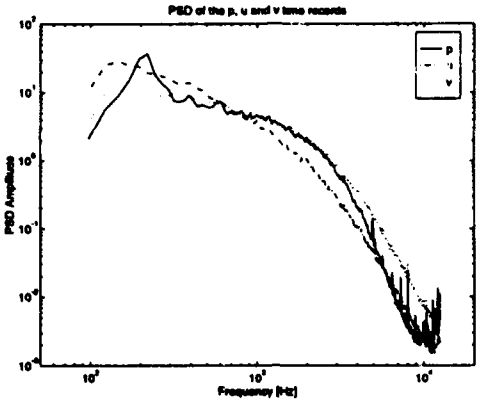

Figure 1.1: The PSD of the u, v and p time records.

1/32" diameter pinhole cap. The cross-wire had a non-dimensional sensing length of 22 viscous units whereas the microphone had a spatial resolution of 34 viscous units.

The presented data were obtained with the hot-wire located at a distance of $y/\delta = 0.08$ ($y^+ = 84$), flow speed of 51 ft/s (15.5 m/s) and $R_\theta = 2945$ ($\delta^+ = 1221$). A detailed description of the wind tunnel facility and the measuring procedures can be found in [7].

The time records of the wall pressure (p), the streamwise velocity (u) and the wall-normal velocity (v) were obtained by antialiasing the sensor signals with 8-pole low-pass elliptic filters with cutoff frequency at 12.5 KHz. The data were digitized at a sampling rate of 25 KHz for 10 seconds. These data records were then filtered and normalized. The filtering was performed digitally using a 5th order Butterworth high-pass filter with the cutoff frequency at 100 Hz. Wilczynski (cf. [7]) showed that high-pass filtering at this frequency did not affect the integrity of the large amplitude events. The normalization was performed with respect to the power present in the resulting sequences, so that the three normalized time records have unit power.

The estimates of the power spectral density (PSD) for p, u and uv are given in figures 1.1 and 1.2. These estimates were computed using Welch's averaged periodogram method. The frequency bump in the p spectrum is due to the shedding from the hot-wire traverse system.

The higher frequency components of the uv record are greater than their

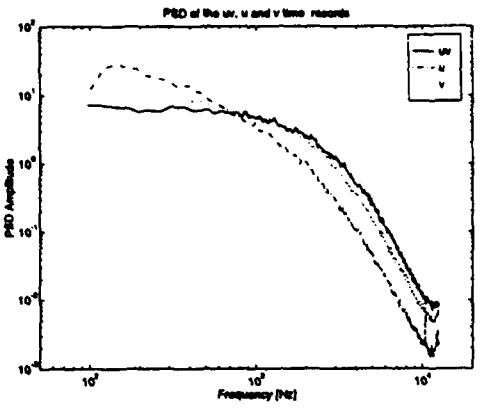

Figure 1.2: The PSD of the u, v and uv time records.

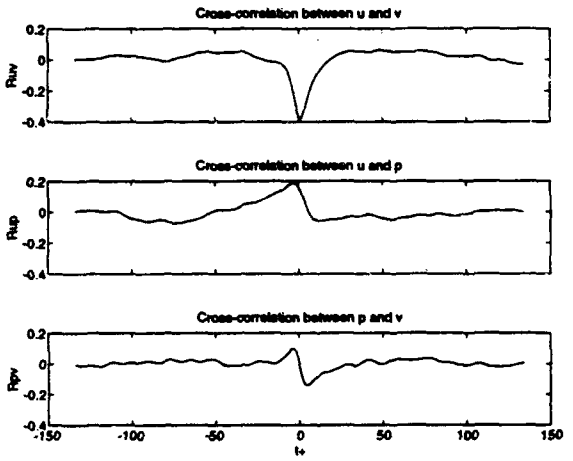

Figure 1.3: The biased cross-correlations between u and v, u and p, and p and v. These computations were performed with 32768 samples of each time record.

equivalent components in the u and v records. This is a consequence of the increase of axis crossings in uv. Note that the roll-off followed by the PSD's of the time records are similar.

The physics of the turbulent flow can be initially seen in the cross-correlation,$R_{xy} = E\{x(t_1)y(t_2)\}$, between the u, v and p time records, as shown in figure 1.3. The biased estimates of the cross-correlations plotted in figure 1.3 show that u is correlated to $-v$ and p only at $t_1 - t_2 \approx 0$. It also shows that p and v are correlated. The cross-correlation results are given as a function of $t^+ = tu_\tau^2/\nu$ where t is the sampling time. A more extensive discussion of the correlation based on cross-spectra data can be found in [5] and [7].

1.3 Objective of the Investigation

A formulation of the problem will be presented prior to the application of time-frequency localization techniques.

The u, v and p time records can be assumed to be random processes of the form

$$u(t) = u_s(t) + u_n(t) \tag{1.1}$$
$$v(t) = v_s(t) + v_n(t) \tag{1.2}$$
$$p(t) = p_s(t) + p_n(t) \tag{1.3}$$

where $u_s(t)$, $v_s(t)$ and $p_s(t)$ are due to active structures in the turbulent flow, and $u_n(t)$, $v_n(t)$ and $p_n(t)$ are assumed to be noise (in general, non-gaussian). It is postulated that u_s and v_s represent the distinct features of organized structures and that $p_s(t)$ represents the unique signatures of these intermittent flow events.

Different schemes could be exercised to isolate the signal from the noise in the time records. This study uses time-frequency localization procedures in an attempt to partition the data as described by equations 1.1 thru 1.3.

Chapter 2 will examine the application of three techniques for the characterization of time records: Short-time Fourier Transforms, Continuous Wavelet Transforms, and Discrete Orthogonal Wavelet Transforms. A filtering technique for the extraction of the signal, based on an orthogonal wavelet

expansion of the temporal records is presented in Chapter 3. A comparative evaluation of event detection between the filtered and unfiltered temporal records is briefly presented in Chapter 4. Finally, a discussion and summary of the findings are included.

Chapter 2

TIME-FREQUENCY LOCALIZATION

The segments of the time records shown in figure 2.1 illustrate the difficulty of objectively identifying organized structures that are common to all the time records. It is possible that in transforming the time records to the frequency domain, or to the time-frequency domain, the structures will become more clearly identifiable. There are several techniques for implementing these alternative representations. The Short Time Fourier Transform and the Wavelet Transform will be examined in this paper. These techniques will be applied to the $u(t)$ record. Similar results have been obtained for $v(t)$, $uv(t) = u(t)v(t)$ and $p(t)$ records.

2.1 Short Time Fourier Transform

The Short Time Fourier Transform (STFT) (cf. [8]) defined as

$$\mathrm{STFT}(t, f) = \int f(\tau) g(\tau - t) e^{-i2\pi f \tau} d\tau \tag{2.1}$$

(with $g(t)$ assumed as a Hanning window) is applied to the interval of u shown in figure 2.1. The magnitude and phase spectrograms of the corresponding STFT are shown in figure 2.2.

Clearly identifiable structures are absent in the spectrograms of figure 2.2. This is also the case for other sections randomly selected from the time

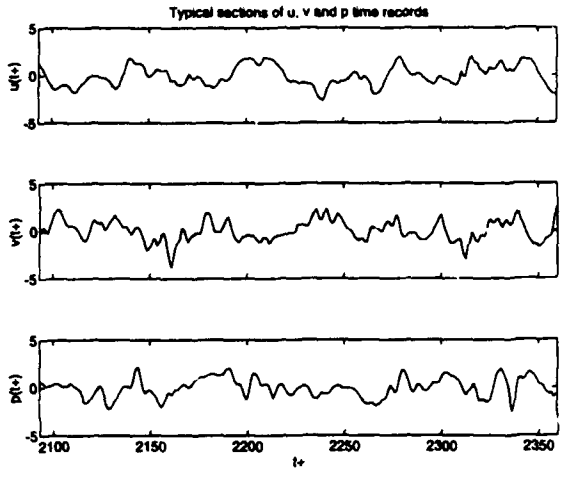

Figure 2.1: Sections of $u(t)$, $v(t)$ and $p(t)$ taken at the same time interval $2093 < t^+ < 2360$.

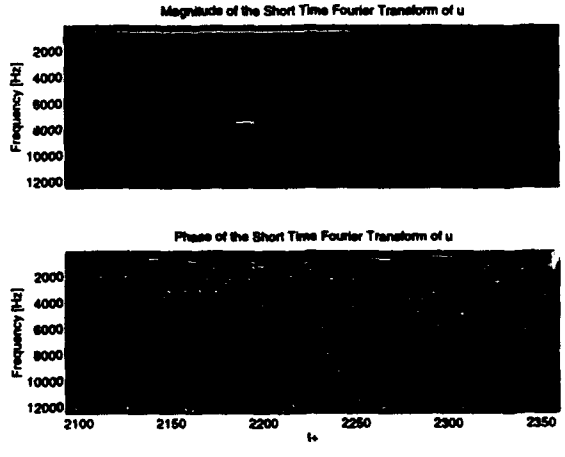

Figure 2.2: Spectrograms of the magnitude and phase of the STFT of $u(t)$ for $2093 < t^+ < 2360$. The maximum and minimum intensity values for the magnitude plot are 70 and 0. The maximum and minimum intensity values for the phase plot are π and $-\pi$.

records. The magnitude spectrogram shows that the main frequency components in the time record are located below 4 KHz, which is already known from the PSD plots in figures 1.1 and 1.2.

Windowed spectra of conditionally sampled events have also been tried without any new insight on the detection problem. The results only confirm the broad spectral range of short-time events. From these preliminary studies, STFT techniques do not appear to be a feasible means for signal identification.

2.2 Continuous Wavelet Transform

A comprehensive review on the theoretical foundation of wavelets is given by Daubechies (cf. [8]), and formed the basis of much of the work to be presented. The applications of wavelet transforms to fluid mechanics and turbulence had been examined by Meneveau [9] ,Farge [10] and Zubair [11].

The Continuous Wavelet Transform (WT) is defined as

$$\mathrm{WT}(a,b) = \int f(\tau)\psi^{a,b}(\tau)d\tau \tag{2.2}$$

where the $\psi^{a,b}(t) = |a|^{-1/2}\psi(\frac{t-b}{a})$ are known as wavelets and $\psi(t)$ is known as the *mother wavelet* since all waveletes are mutually similar with a dilation or scaling parameter a. Individual wavelets are characterized by three features; shape, duration and location (cf. [12]). A wide range of both continuous and discrete wavelets exists and the selection dictates the shape. The parameter b defines the location along the temporal axis, while a is associated with the duration. It should be noted that decreasing values of a correspond to wavelets with higher amplitude and shorter duration.

An equivalent expression for the Wavelet Transform can be formulated in terms of the Fourier Transforms for the signal ($\hat{f}(\omega)$) and wavelets ($\hat{\psi}(a\omega)$) as follows

$$\mathrm{WT}(a,b) = \sqrt{a}\int_{-\infty}^{\infty} \hat{f}(\omega)\hat{\psi}(a\omega)e^{ib\omega}d\omega. \tag{2.3}$$

This expression illustrates that the wavelet decomposition acts as a filtering of $\hat{f}(\omega)$ by $\sqrt{a}\hat{\psi}(a\omega)$ with a phase lag $b\omega$. For most practical applications, wavelets are well-localized in both time and frequency. In addition, wavelet filters have constant *relative* bandwith ($\Delta\omega/\omega = Constant$) in contrast to the constant bandwidth of the STFT.

A discussion comparing STFT and Wavelet Transforms is presented by Daubechies (cf. [8]). She explains that the essential difference between wavelets and windowed Fourier transforms is in the shape of the windowed function. The STFT consists of a $g(t)$ function with constant bandwidth, translated to the proper location, and *filled in* with high frequency oscillations. Wavelets $\psi^{a,b}(t)$ are a family of prescribed shapes that are also translated, but compressed or stretched. The time widths are adapted to their frequency bands; wavelets with high-frequency components are very narrow while, wavelets with low-frequency components are much broader. As a result, the wavelet transform is better able than the windowed Fourier transform to *zoom in* on very short-lived high frequency phenomena, such as transients in signals.

The scalograms shown in figure 2.3 were computed from the $u(t)$ data record using (2.2) and the Morlet wavelet $\psi(t) = Ce^{-t^2/\alpha^2}(e^{i\pi t} - e^{-\pi^2\lambda^2/4})$ with $\alpha = 6/5$, $C = 1$ and $\lambda \gg 2/\pi$. These scalograms do not show distinct concentrations of energy that could be unequivocally identified. Real wavelets, like the First Derivative of the Gaussian, $\psi(t) = -te^{-t^2/2}$, or the Second Derivative of the Gaussian (known also as the *Mexican Hat*), $\psi = (1 - t^2)e^{-t^2/2}$, give equivalent results as illustrated in figure 2.4. Liandrat et al [13] obtained similar results to those shown in figure 2.4 for the *Mexican Hat*. They suggested that shaded cone-like structures in the scalogram correspond to ejections/sweep events. A comparison between their wavelet results and VITA detection showed reasonable agreement.

2.3 Discrete Orthogonal Wavelet Transform

2.3.1 Basic Concepts

Similar to the Fast Fourier Transform (FFT), Discrete Orthogonal Wavelet Transform can be formulated. For this case, a particular set of wavelets is specified by a discrete set of wavelet (filter) coefficients. Several families of orthogonal wavelets with compact support have been defined in the literature Fast algorithms have been developed for the computation of these wavelets (cf. [14]). Zubair [11] utilized a new class of algorithms, called wavelet-packets. This procedure segments the turbulence data adaptively and selects the best basis from a large collection of wavelets. Intuitively, it represents the wavelets expansion with the least number of coefficients.

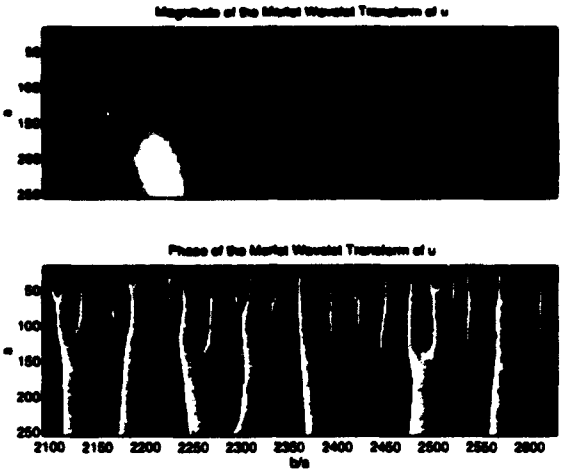

Figure 2.3: Scalograms of the magnitude and phase of the Morlet WT of $u(t)$ for $2093 < t^+ < 2360$. The Morlet wavelet has $\alpha = 6/5$ and $C = 1$. The maximum and minimum intensity values for the magnitude plot are 2.4e+05 and 32. The maximum and minimum intensity values for the phase plot are π and $-\pi$.

This study is restricted to the application of three wavelet families, two of them constructed by I. Daubechies (*Extremal Phase*, and *Least Asymmetric*), and one formulated by R. Coifman and documented by I. Daubechies (*Coiflets*) (cf. [8]). These are denoted as:

- D8 — Daubechies Extremal Phase 8-coefficients,
- L8 — Daubechies Least Asymmetric 8-coefficients,
- C18 — Coiflets 18-coefficients.

The Fast Wavelet Transform (FWT) of a one dimensional time record containing 2^N samples is a vector of length 2^N. In order to compute a FWT, the number of samples in the time record must be a power of two (cf. [14]). This is not a severe limitation because the time records can be conveniently zero padded. The u, v and p records used in this analysis contain 249000 samples (digitized at 25000 samples per second). The corresponding zero padded sequences contain $2^{18} = 262144$ samples.

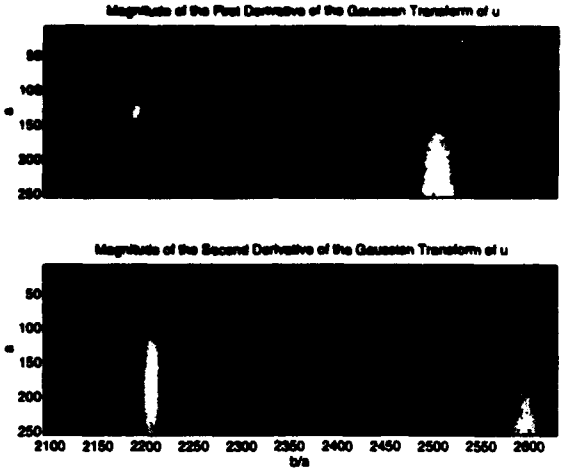

Figure 2.4: Scalograms of the First and Second Derivatives of the Gaussian WT of $u(t)$ for $2093 < t^+ < 2360$. The maximum and minimum intensity values for the First Derivative WT plot are 426 and -588. The maximum and minimum intensity values for the Second Derivative WT plot are 335 and -290.

Discrete Orthonormal wavelets with indices m, n are defined as

$$\psi^{m,n}(t) = \frac{1}{\sqrt{a_m}}\psi\left(\frac{t - b_n}{a_m}\right) = \frac{1}{2^{m/2}}\psi(2^{-m}t - n2^{-m}) \tag{2.4}$$

where $a_m = 2^m$ and $b_n = n$.

A function $f(t)$ is represented by the wavelet expansion with coefficients C_ℓ where $0 \leq \ell \leq 2^N - 1$. The index ℓ is related to m, n by means of a dyadic pattern in the m, n plane (figure 2.5). There are N rows of coefficients denoted by $1 \leq m \leq N$. For each row m there are 2^{N-m} coefficients, therefore the range of n in that row is $1 \leq n \leq 2^{N-m}$. The index $\ell = 1$ corresponds to $m = N$ and $n = 1$, the single element row. When displaying the wavelet coefficients with increasing index ℓ, they are grouped in row intervals $2^{(k-1)} \leq \ell \leq 2^k - 1$ with $k = N - m + 1$ and $1 \leq k \leq N$. The number of terms in each row k doubles sequentially.

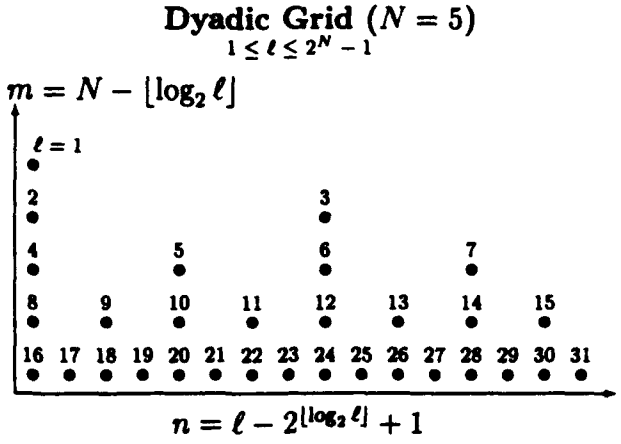

Figure 2.5: Dyadic Arrangement of Wavelet Coefficients

2.3.2 Example using the D8 wavelet transform

The features of discrete wavelets and the dyadic grid expansion will be illustrated primarily for the D8 wavelets with a data record of length 2^N for $N = 18$.

Figure 2.6 shows some of the orthogonal wavelet functions for different values of m and n. It should be observed that the scaling factor $a_m = 2^m$ controls not only the time duration of the wavelet, but also its energy. Therefore, the peak amplitude of short wavelets (for instance, $m = 4$) is higher than the peak amplitude of long wavelets (for instance $m = 6$). The normalized magnitudes of the FFT's corresponding to the wavelets in figure 2.6 are shown in figure 2.7 and illustrates the constant relative bandwidth ($\Delta\omega/\omega$) of the wavelet filters. It should also be noted that the sequential terms in the wavelet expansion will have overlapping frequency bands, particularly in the high frequency groups. This is in contrast to traditional band-pass filtering techniques [14].

For this example (with $N = 18$), the dyadic arrangement of the coefficients C_ℓ for $1 \le \ell \le 262143$ can be summarized in tabular form. Table 2.1 lists the number of terms in each of the m rows of the dyadic pattern; the center frequency f_c (computed for D8 wavelets) for those terms in the respective rows; and the time interval T^+ between the n wavelets stretched along the time record (as shown in figure 2.6). It should be noted that the scaling

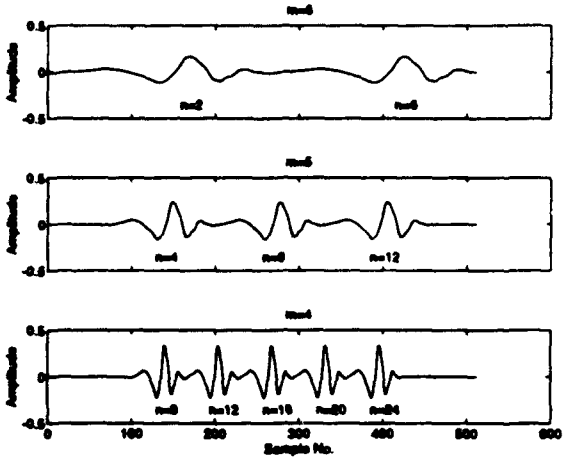

Figure 2.6: Daubechies Extremal Phase orthogonal base functions computed with FIR filters having 8 coefficients.

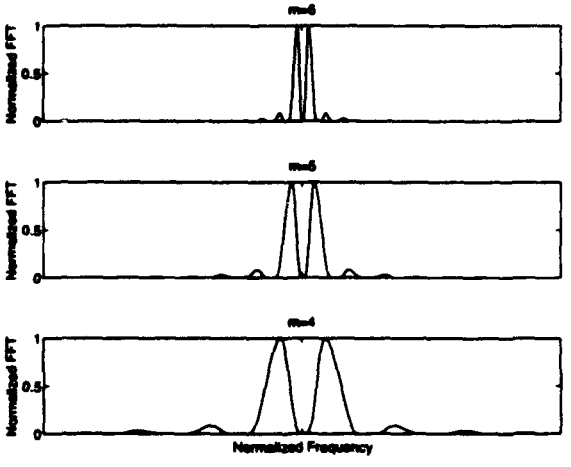

Figure 2.7: Normalized FFT magnitude of the Daubechies Extremal Phase orthogonal base functions of figure 2.6.

	m	k	Range of ℓ	# of terms per row	$\mathcal{D}8$ f_c [Hz]	$a = 2^m = T^+$
	18	1	$\ell = 1$	1	-	262144
	17	2	$2 \leq \ell \leq 3$	2	-	131072
	16	3	$4 \leq \ell \leq 7$	4	-	65536
	15	4	$8 \leq \ell \leq 15$	8	-	32768
	14	5	$16 \leq \ell \leq 31$	16	-	16384
	13	6	$32 \leq \ell \leq 63$	32	1	8192
	12	7	$64 \leq \ell \leq 127$	64	2	4096
	11	8	$128 \leq \ell \leq 255$	128	4	2048
	10	9	$256 \leq \ell \leq 511$	256	9	1024
	9	10	$512 \leq \ell \leq 1023$	512	17	512
	8	11	$1024 \leq \ell \leq 2047$	1024	34	256
•	7	12	$2048 \leq \ell \leq 4095$	2048	68	128
•	6	13	$4096 \leq \ell \leq 8191$	4096	136	64
•	5	14	$8192 \leq \ell \leq 16383$	8192	272	32
•	4	15	$16384 \leq \ell \leq 32767$	16384	545	16
•	3	16	$32768 \leq \ell \leq 65535$	32768	1090	8
	2	17	$65536 \leq \ell \leq 131071$	65536	2181	4
	1	18	$131072 \leq \ell \leq 262143$	131072	4363	2

Table 2.1: Grouping of wavelet coefficients for a dyadic grid with $N = 18$. The energy of $u(t)$, $v(t)$ and $p(t)$ records is concentrated in bands marked with • symbol

factor $a_m = 2^m$ is equal to the time interval T^+.

Let $\Psi(\omega)$ be the Fourier Transform of the mother wavelet. Then it can be shown that the Fourier Transform of $\psi^{m,n}(t)$ is proportional to $\Psi(\omega/2^m)$. It is clear that the center frequency f_c of a wavelet in row m is related to the center frequency f_0 of the mother wavelet through $f_c = f_0/2^m = f_0/T^+$. Since $m = N - k + 1$, then $f_c = (2^k/2^{N+1})f_0$ or $f_c/f_s = A2^k$ where A is a proportionality constant and f_s is the sampling frequency. Thus f_c doubles sequentially for each row k as shown in Table 2.1. This sequence of frequencies can, to a first approximation, be equated to the Fourier frequency. The assumption being that the overlapping bands are not significant.

As an illustration of the magnitude of the coefficients for a typical signal, the $u(t)$ temporal record was analyzed by means of the wavelet expansion. Two wavelet families were examined; D8-Daubechies Extremal Phase and L8-Daubecies Least Asymmetric. For purposes of graphical display $N = 15$ was chosen. Figure 2.8 shows the time record and the magnitudes of the coefficients C_ℓ for $1 \leq \ell \leq 32767$ for D8 and L8 wavelet expansions. The last row with the highest concentration of coefficients ($m = 1$ or $k = 15$) has the coefficient indices $2^{14} \leq \ell \leq 2^{15} - 1$. The magnitudes of these coefficients are relatively small.

It will be shown in subsequent results that only approximately 10% of the coefficients are needed to represent the signal and for this application are dominated by terms in the expansion for $2 \leq m \leq 8$. This covers the center frequency range $34 \leq f_c \leq 2181$, which is not surprising in view of the spectral content of the time records shown in figure 1.1.

The energy of the time record can be computed from the wavelet coefficients by application of Parseval's theorem. When the basis wavelet functions are orthonormal, the expected value of the signal energy is given by the mean square value of the wavelet coefficients. The Power contained in each row of the expansion can be correlated with the center frequency of the wavelets contained in the respective rows. Figure 2.9 displays the Power versus f_c for the D8 wavelets. As shown in the figure, the shape of this curve does not approximate the spectral curves of $u(t)$. These results offer a poor approximation to the spectral content of the time records because the center frequency only represents the location of the frequency bands which, as previously discussed, have extensive overlapping.

A more meaningful wavelet spectrum that accounts for the overlap has been formulated by Zubair [11]. The energy spectrum of the wavelet-coefficients

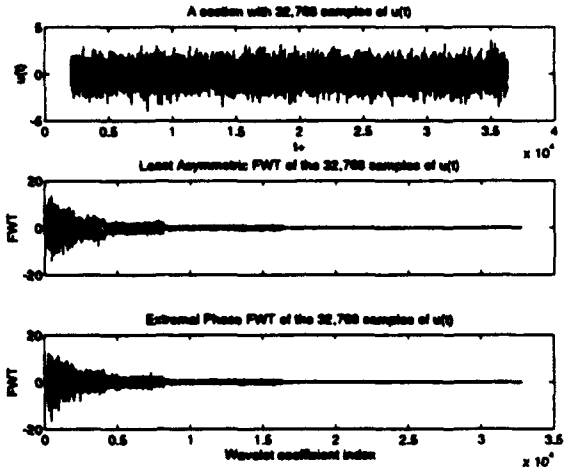

Figure 2.8: Least Asymmetric and Extremal Phase FWT's of $u(t)$.

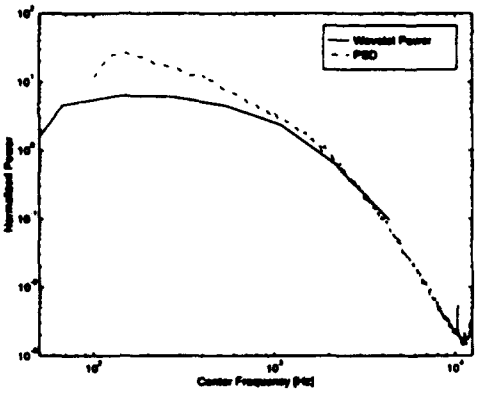

Figure 2.9: Wavelet Power versus Center Frequency for the D8 wavelets and the $u(t)$ record.

is segmented into bins. The wavelet-spectrum is found by adding the energy contributions from all the wavelet coefficients contained in each of the bins.

Chapter 3

APPLICATION OF WAVELET FILTERING

Traditional bandpass filtering techniques based on Fourier decomposition have often been used to investigate intermittent turbulent structures. These techiques have had limited success and often present a biased viewpoint on the scales of turbulence. Wavelet filtering offers a promising new approach to this problem.

Zubair [11] examined the application of wavelet transforms, including spectral analysis and filtering, to several aspects of turbulent flows. He developed a wavelet power-spectra and filtering technique analogous to Fourier techniques to interpret the scale-based behavior of turbulence. His conclusion is that wavelet-packet filtering is an improvement over Fourier filtering by providing sharper separation between bands of scales, and thus offering more sensitivity than Fourier filtering. However, his results on three facets of the structure of turbulence — local itotropy, intermittency and scaling of structure functions — showed only modest improvement over Fourier filtering.

3.1 Conventional Wavelet Filtering

A wavelet filter, based on an orthogonal wavelet expansion, can be implemented by first sorting the wavelet coefficients in decreasing magnitude order; and then zeroing out all the coefficients with magnitude lower than a speci-

fied threshold (cf. [14]). The limit can be set so that the energy contained in the filtered sequence is a fraction of the total energy. Let k_f be the fraction of the total signal energy that is present in the filtered sequence, then

$$E\{y_w^2(t)\} = k_f E\{y^2(t)\} \tag{3.1}$$

where $y(t)$ represents $u(t)$, $v(t)$ or $p(t)$. The wavelet-filtered time record can be reconstructed by computing the inverse fast wavelet transform (IFWT) of the remaining wavelet coefficients. The discussion will focus on the $u(t)$ time record. However, all three time records were analyzed.

The performance of the described wavelet filter depends on the wavelet basis and the value of k_f. There are many families of wavelets that could be chosen for the implementation of the wavelet filter.

Let $u_w(t)$ be the wavelet filtered sequence of $u(t)$, then,

$$u(t) = u_w(t) + u_{w_n}(t) \tag{3.2}$$

where $u_{w_n}(t)$ represents the noise present in the filtered sequence. As a first approximation, assume that the overall shape of the PSD of $u(t)$ is determined mainly by the presence of organized turbulent structures. A wavelet selection is made by choosing the wavelet basis for which the PSD of $u_w(t)$ most closely matches the PSD of $u(t)$. Three families of wavelets will be examined.

The first example uses a wavelet filter constructed with the 8-coefficient Daubechies Extremal Phase (D8) wavelet basis (cf. [8, page 194]). The PSD's of $u(t)$, $u_w(t)$ and $u_{w_n}(t)$ for $k_f = 0.9$ are shown in figure 3.1.

For the second example, the wavelet filter is implemented with the 18-coefficient Coiflet (C18) wavelet basis (cf. [8, page 261]) and $k_f = 0.9$. The corresponding PSD's are shown in figure 3.2.

For the third example, the wavelet filter is implemented with the 8-coefficient Daubechies Least Asymmetric (L8) wavelet basis (cf. [8, page 198]) and $k_f = 0.9$. The corresponding PSD's are shown in figure 3.3.

The three examples show that the overall shapes of the PSD's of $u(t)$ and $u_w(t)$ are not preserved in the high frequency range. However, it should be noted that the PSD's of $u_w(t)$ in the three examples have similar shapes. It appears that the PSD of the wavelet-filtered record is independent of the choice of wavelet basis.

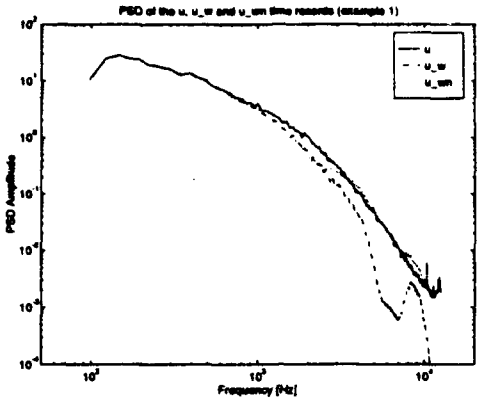

Figure 3.1: PSD of $u(t)$, $u_w(t)$ and $u_{w_n}(t)$. The sequence $u_w(t)$ was obtained using the D8 wavelet filter with $k_f = 0.9$

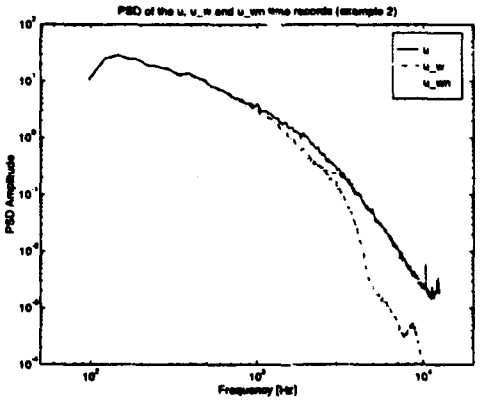

Figure 3.2: PSD of $u(t)$, $u_w(t)$ and $u_{w_n}(t)$. The sequence $u_w(t)$ was obtained using the C18 wavelet filter with $k_f = 0.9$

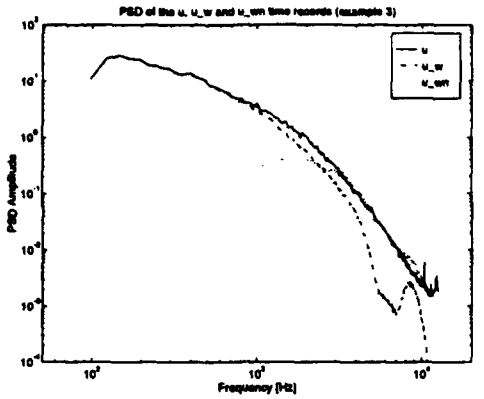

Figure 3.3: PSD of $u(t)$, $u_w(t)$ and $u_{w_n}(t)$. The sequence $u_w(t)$ was obtained using the L8 wavelet filter with $k_f = 0.9$

It is instructive to examine the data compression achieved by the wavelet filter. From the 262144 wavelet coefficients obtained from the zero padded $u(t)$ time record, only 20373 coefficients are used to reconstruct $u_w(t)$ in the first example, 19672 coefficients are used in the second example, and 20367 in the third example. In all cases, less than 10% of the coefficients are retained, therefore, significant data compression has been achieved. The fact that the number of wavelet coefficients is lower in the second example is an indication that the signal energy for this case is slightly more concentrated in wavelet space.

Segments of the $u(t)$ and $u_w(t)$ data records are shown in figure 3.4 for the three examples. There is little difference between the original and the filtered records because only 10 percent of the original energy has been removed.

These conventional wavelet filters have effects similar to that of a low-pass filter. Values of k_f closer to one cause a shift of the equivalent cutoff frequency towards higher frequencies. Lower values of k_f cause a shift of the equivalent cutoff frequency towards lower frequencies. The natural question that arises is: what is the difference between this filter and the traditional low-pass filters in the frequency domain? One way to resolve this issue is to select a classical filter that would produce effects similar to the ones seen in figures 3.1 to 3.3. A lowpass Butterworth filter of first order with cutoff frequency at 2 KHz will produce the least steep rolloff in the PSD of the filtered sequence. The

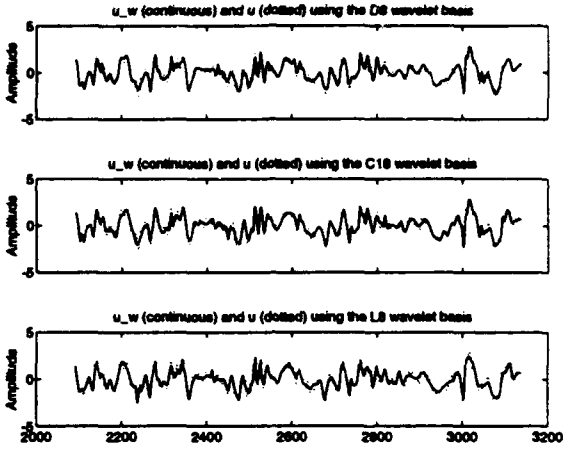

Figure 3.4: Segments of the $u(t)$ and $u_w(t)$ time records for the wavelet filters described in examples 1 (D8), 2 (C18) and 3 (L8).

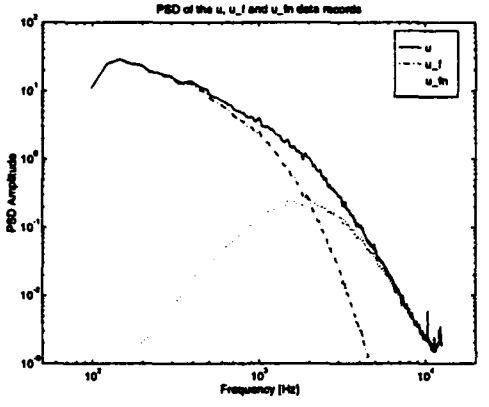

Figure 3.5: PSD of $u(t)$, $u_f(t)$ and $u_{f_n}(t)$. The sequence $u_f(t)$ was obtained using a first order Butterworth filter (double pass for phase compensation) with cutoff frequency at 2000 Hz.

filter order is effectively doubled by forward and reverse filtering to provide phase compensation. Using a notation consistent with (3.2), let $u_f(t)$ be the butterworth filtered sequence of $u(t)$, then,

$$u(t) = u_f(t) + u_{f_n}(t) \tag{3.3}$$

where $u_{f_n}(t)$ represents the noise present in the filtered sequence. The resulting PSD's are shown in figure 3.5.

Butterworth filters of higher order produce a rolloff steeper than the one shown in figure 3.5. This effect is not desired if the shape of the PSD is to be preserved. An increase in the cutoff frequency causes less distortion in the PSD, however, the effect of filtering decreases because the noise remains present in the filtered record.

The wavelet filter appears to affect the data in a range of frequencies that vary from low frequencies to high frequencies, while the effect of the Butterworth filter is concentrated in the higher frequencies.

3.2 Weighted Wavelet Filtering

To extend the effects of the wavelet filter to a wider frequency range, a weight $w(m)$ can be assigned to the rows of the wavelet coefficients so that those coefficients associated with a common scaling factor $a = 2^m$ have the same weight. For instance, in a sequence having 2^N samples, the weight could be set to $w(m) = 2^{-\alpha m}$. Figure 3.6 shows three examples of the effect of multiplying the D8 FWT coefficients of $u(t)$ by its associated weights $w(m) = 1$, $w(m) = 2^{-m/2}$ and 2^{-m} (using $\alpha = 0$, $\alpha = 1/2$ and $\alpha = 1$, respectively). Similar results were found using C18 and L8 FWT's.

The modified wavelet filter is constructed as it is initially described, with the exception that the sorted descending ordering is applied to the weighted wavelet coefficients. It should be noticed that the weighting scheme is used only to determine which coefficients are selected. The selected coefficients do not undergo any modification.

In order to examine the effects of the weighting scheme on the selection of the coefficients C_ℓ, the segment of the total wavelet power contained in each row m of the coefficient expansion will be evaluated. The weighting $w(m)$ alters the selection of the individual terms in each row and thus the frequency content of the filtered signal. Figures 3.7, 3.8 and 3.9 show the

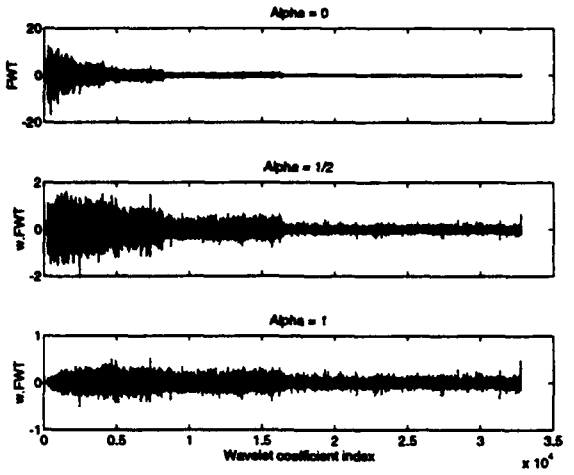

Figure 3.6: Effects of the weights $w(m) = 1$ (top), $w(m) = 2^{-m/2}$ (middle) and $w(m) = 2^{-m}$ (bottom) applied to the D8 FWT coefficients of $u(t)$. A segment of the $u(t)$ record containing $2^N = 32768$ was used in the computations.

signal energy versus m for the three examples of figure 3.6. The filter was constructed for $k_f = 1, .9., .7,$ and $, .5$.

As previously stated, the wavelet coefficients that dominate the signal are terms in rows $2 \leq m \leq 8$ with center frequencies $2181 \geq f_c \geq 34$, respectively. The results indicate that:

- The weighting $w(m) = 1$ (conventional filtering) crudely approximates a low-pass filter — as previously discussed — by mostly eliminating coefficients in rows $2 \leq m \leq 6$ associated with wavelets that have high frequency components.
- The weighting $w(m) = 2^{-m/2}$ approximates a bandpass filter by eliminating coefficients associated with wavelets containing both high and low frequency components.
- The weighting $w(m) = 2^{-m}$ approximates a high-pass filter by eliminating coefficients in rows $5 \leq m \leq 8$ associated with wavelets that have low-frequency components.

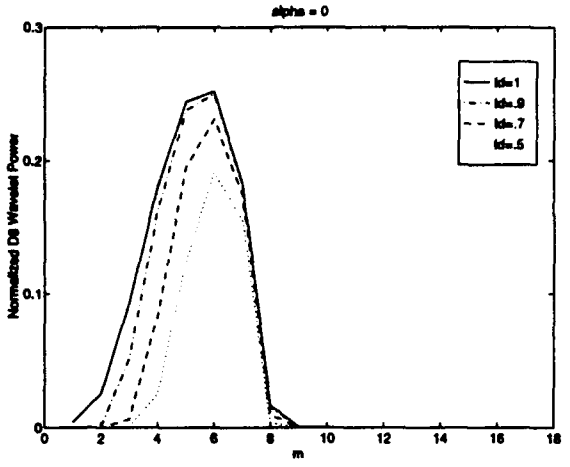

Figure 3.7: Normalized D8 Wavelet Power versus m for $w(m) = 1$ ($\alpha = 0$) and $k_f = 1, .9, .7$ and $.5$

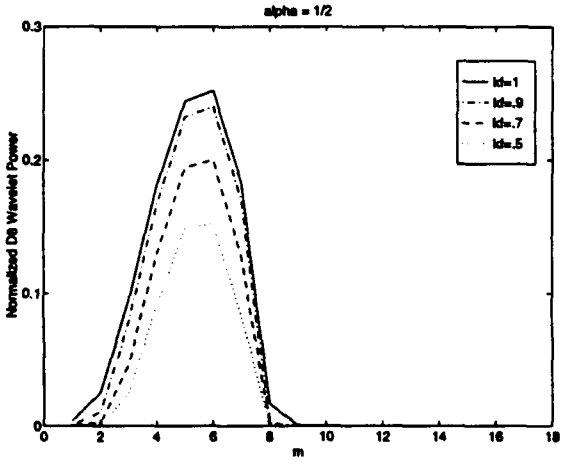

Figure 3.8: Normalized D8 Wavelet Power versus m for $w(m) = 2^{-m/2}$ ($\alpha = 1/2$) and $k_f = 1, .9, .7$ and $.5$

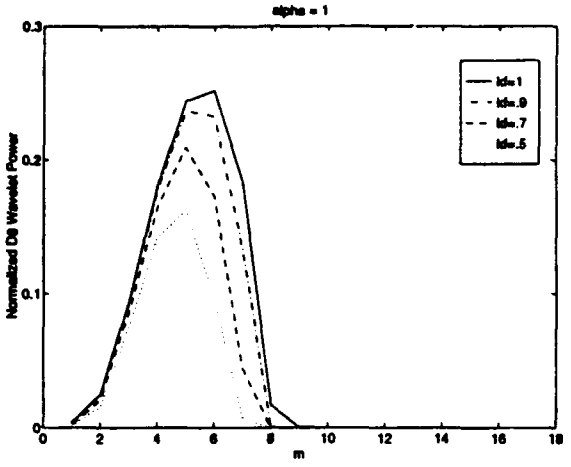

Figure 3.9: Normalized D8 Wavelet Power versus m for $w(m) = 2^{-m}$ ($\alpha = 1$) and $k_f = 1, .9, .7$ and $.5$

This is more clearly displayed in figures 3.10, 3.11 and 3.12 where the PSD's of the reconstructed filtered signals are shown. These figures correspond to the three weighting schemes for $k_f = .5$. Similar results were obtained for other values of k_f.

As a first attempt at designing a wavelet filter, extensive computations were made utilizing the three weighting schemes discussed above. The techniques were applied simultaneously to $u(t)$, $v(t)$, and $p(t)$ time records at several locations across the turbulent boundary layer.

A wavelet filter constructed using D8 with $w(m) = 2^{-m/2}$ and $k_f = 0.7$ will be used to illustrate the effect of weighted filtering. This filter was chosen because it best preserves the overall spectrum shape while eliminating energy from both low and high ends of the spectrum. The time record of unfiltered and filtered signals for $u(t)$, $v(t)$ and $p(t)$ at the near wall location $y/\delta = 0.08$ are shown in figure 3.13. The filtered sequences are smoother than the original signal, primarily because of the low-pass effect of the filter. It also appears that the peak events are preserved in the filtered record. The next Chapter will perform further analyses of this filter scheme based on conditional sampling of both the filtered and unfiltered time records.

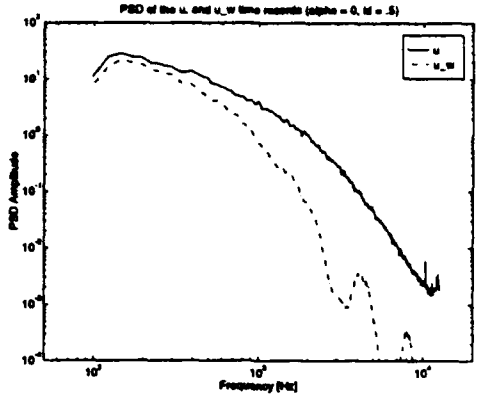

Figure 3.10: PSD of $u(t)$ (solid) and $u_w(t)$ (dashed) for $k_f = .5$ and $w(m) = 1$ ($\alpha = 0$)

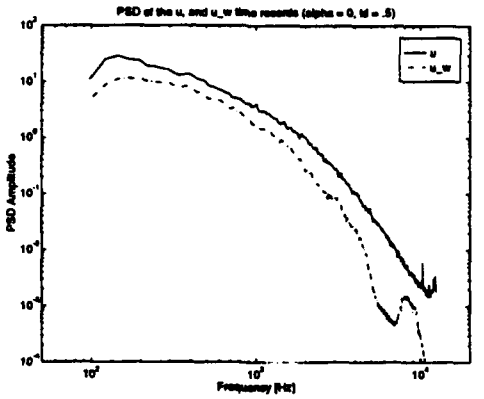

Figure 3.11: PSD of $u(t)$ (solid) and $u_w(t)$ (dashed) for $k_f = .5$ and $w(m) = 2^{-m/2}$ ($\alpha = 1/2$)

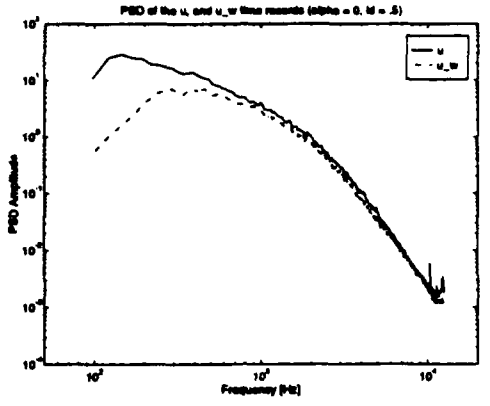

Figure 3.12: PSD of $u(t)$ (solid) and $u_w(t)$ (dashed) for $k_f = .5$ and $w(m) = 2^{-m}$ ($\alpha = 1$)

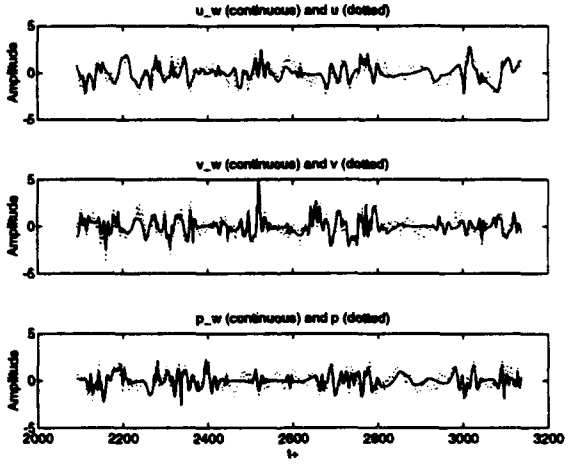

Figure 3.13: Segments of $u(t)$, $u_w(t)$, $v(t)$, $v_w(t)$, $p(t)$ and $p_w(t)$. The sequences $u_w(t)$, $v_w(t)$ and $p_w(t)$ were obtained using the D8 modified wavelet filter with $k_f = .7$ and $w(m) = 2^{=m/2}$.

Chapter 4

EVALUATION OF EVENT DETECTION

An initial attempt to evaluate the filtered results will be based on event detection and conditional sampling. A preliminary study of the effect of the wavelet filter on the VITA+ slope event detection method will be presented.

The VITA events of the $u(t)$ sequence require the evaluation of (4.1).

$$\hat{u}(t_0, T_v) = \frac{1}{T_v} \int_{t_0 - \frac{T_v}{2}}^{t_0 + \frac{T_v}{2}} u^2(t_0 + \tau) d\tau - \left\{ \frac{1}{T_v} \int_{t_0 - \frac{T_v}{2}}^{t_0 + \frac{T_v}{2}} u(t_0 + \tau) d\tau \right\}^2 \tag{4.1}$$

A VITA event is detected if $\hat{u}(t_0, T_v) > k_v u_{\text{rms}}^2$. The VITA parameters used in this Chapter are $k_v = 1$, and T_v corresponding to 24 consecutive samples.

The +slope events are detected when the following condition is true

$$\frac{2}{T_s} \int_{t_0}^{t_0 + \frac{T_s}{2}} u(t_0 + \tau) d\tau - \frac{2}{T_s} \int_{t_0 - \frac{T_s}{2}}^{t_0} u(t_0 + \tau) d\tau > 0 \tag{4.2}$$

The T_s parameter was set equal to T_v.

VITA+slope events are usually found by performing an AND operation of the VITA events with the +slope events. However, in order to avoid the double count of a VITA event that coexists with two different +slope events

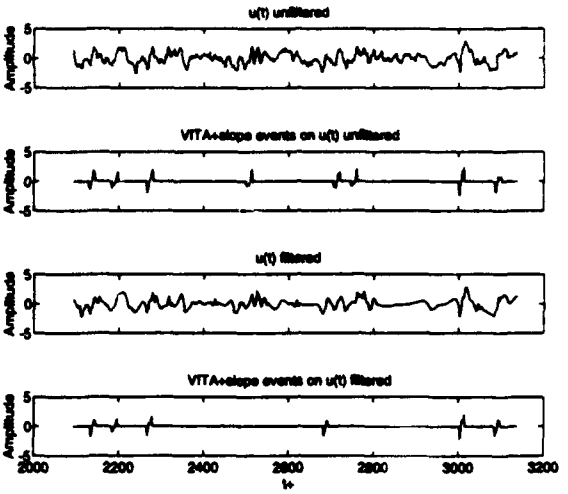

Figure 4.1: Segment of $u(t)$ (upper), VITA+slope events detected on $u(t)$ (middle), and VITA+slope events detected on $u_w(t)$.

(or vice-versa), a VITA+slope event is defined as a +slope event that coexists with one or more VITA events.

The application of the VITA+slope detection scheme results in the detection of 1568 events when it is applied to the $u(t)$ sequence, and 1576 events when it is applied to the $u_w(t)$ sequence. Figure 4.1 shows a section of the u(t) record and the VITA+slope events detected using the original and filtered sequences.

Let $q_2(t)$ and $q_4(t)$ be defined by

$$q_2(t) = \begin{cases} u(t)v(t) & \text{if } u(t) < 0 \text{ and } v(t) > 0 \\ 0 & \text{otherwise} \end{cases} \tag{4.3}$$

$$q_4(t) = \begin{cases} u(t)v(t) & \text{if } u(t) > 0 \text{ and } v(t) < 0 \\ 0 & \text{otherwise} \end{cases} \tag{4.4}$$

The average shape of the VITA+slope events detected on the $u(t)$ record can be found by averaging all the events centered within a window of constant size. The average shapes of the $u(t)$, $v(t)$, $uv(t)$, $q2(t)$ and $q4(t)$ obtained in this way are plotted in figures 4.2 and 4.3. The equivalent processing performed in the filtered sequences (using the events detected by the VITA+slope scheme on the $u_w(t)$ record) are given in figures 4.4 and 4.5.

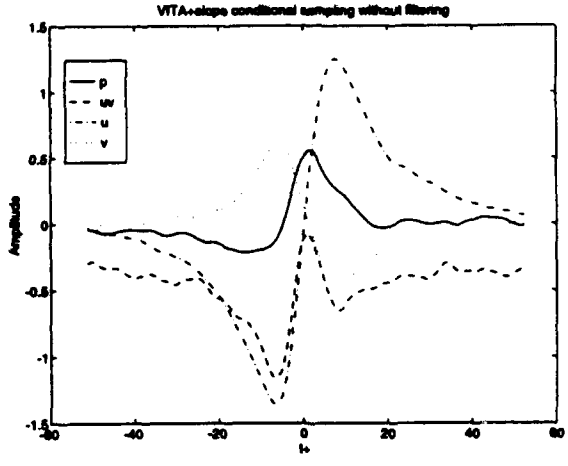

Figure 4.2: Average shape of $p(t)$,$u(t)$, $v(t)$ and $uv(t)$ for VITA+slope events detected on $u(t)$

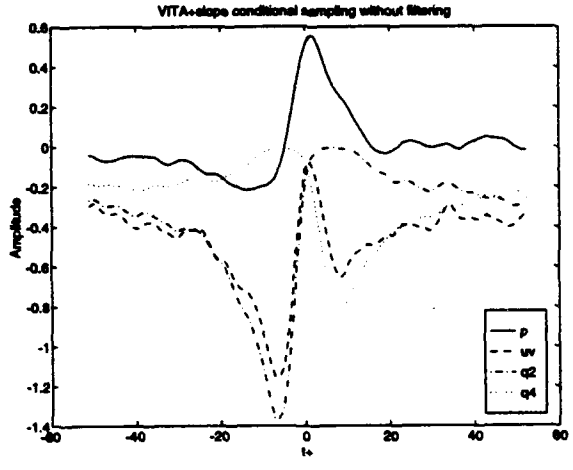

Figure 4.3: Average shape of $p(t)$,$q_2(t)$, $q_4(t)$ and $uv(t)$ for the conditional sampling scheme performed on the VITA+slope events detected on $u(t)$

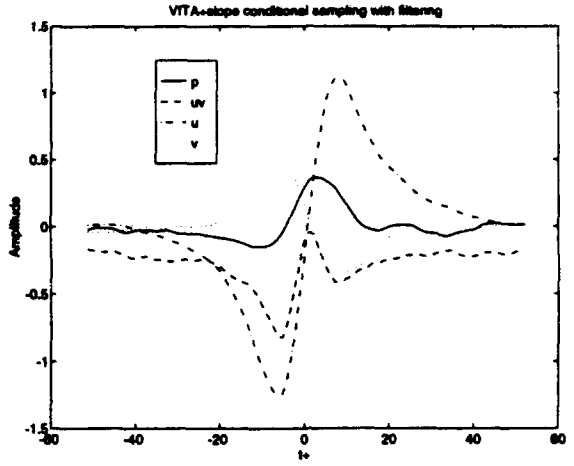

Figure 4.4: Average shape of $p_w(t)$,$u_{w_2}(t)$, $v_w(t)$ and $uv_w(t) = u_w(t)v_w(t)$ for VITA+slope events detected on $u_w(t)$.

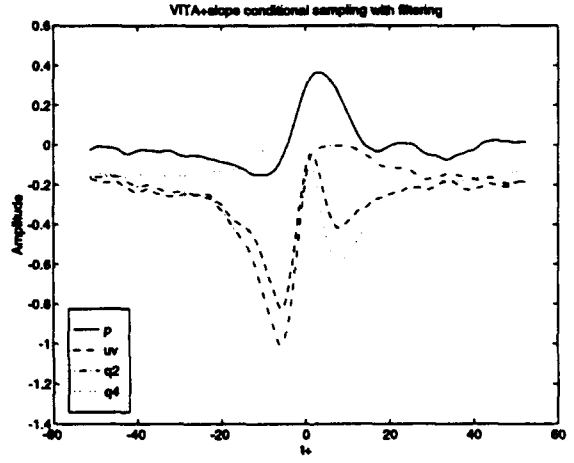

Figure 4.5: Average shape of $p_w(t)$,$q_{2_w}(t)$, $q_{4_w}(t)$ and $uv_w(t) = u_w(t)v_w(t)$ for the conditional sampling scheme performed on the VITA+slope events detected on $u_w(t)$.

In all cases the conditional sampling results are consistent even though only 70% of the original signal energy is present in the filtered records.

Chapter 5

SUMMARY AND DISCUSSION

The fundamental problem posed in this investigation is to separate the signal from the noise in the temporal records defined in (1), (2) and (3). Extensive knowledge of the signal model is a requirement for the design of efficient filters. However, the signal model for this problem is not known.

Conventional spectral filtering does not preserve the integrity of the signal because of the low signal-to-noise-ratio in the frequency band of interest.

Some time-frequency localization techniques have been presented that offer a distinct perspective on the formulation of the problem. The STFT and the Morlet, First and Second Derivatives of the Gaussian Wavelets have been applied to turbulent and wall-pressure time records. The corresponding phase and magnitude spectrograms and scalograms do not contain clearly indentifiable patterns that could lead to a reliable identification of the signal embedded in the noise.

The FWT is a discrete orthogonal wavelet expansion that does not introduce the redundancies of both the STFT and the continuous non-orthogonal Wavelets. It also has a structure that can be used for the systematic discrimination of frequency bands.

A filtering technique based on the FWT was developed. A weighting scheme that allows a systematic selection of the wavelet coefficients is introduced. One of the effects of the selected weights is to preserve the shape of the signal PSD, which is attributed to the existence of large amplitude events.

An evaluation of the proposed filter was performed using conditional sampling based on VITA+slope detection on the u filtered and unfiltered records. The results indicate that the filtered sequences preserve the events while eliminating some of the high and low frequency components. As a result, the process of scanning the filtered data records becomes a possibility in the search of tentative signal models.

Research is now underway to examine other weighting techniques and the subsequent effect on the filtered temporal records. Furthermore, in Part II of this research investigation, filtering techniques will be utilized for the detection of groups or clusters of burst events which are associated with the passage of a single large-scale flow structure. This problem requires a different approach to wavelet filtering and sampling. New data records are also being acquired for disturbed flows.

ACKNOWLEDGEMENTS

This work was supported by the Office of Naval Research with Dr. L. Patrick Purtell as scientific officer, under Grant # N00014-88-K-0141.

The data records used in this phase of the investigation were acquired by Dr. Vincent Wilczynski. The authors are grateful for his cooperation.

Bibliography

[1] Robinson, S.K.," Coherent Motions in the Turbulent Boundary Layer," Ann. Rev. of Fluid Mech., vol. 23, pp. 601–639, 1991.

[2] Farabee, T. M. and Casarella, M.J., "Spectral Features of Wall Pressure Fluctuations Beneath Turbulent Boundary Layers," Phys. Fluids A, Vol 3, No. 10, pp. 2410–2420, 1991.

[3] Kim, J., "On the Structure of Pressure Fluctuations in Simulated Turbulent Channel Flow," J. Fluid Mech., No. 205, pp. 421–451, 1989.

[4] Wilczynski, V., Casarella, M.J. and Kammeyer, M., "A Comparison of Data on Intermittent Turbulent and Wall Pressure Events," ASME Winter Meeting, NCA-Vol 15, FED-Vol 168, 1993.

[5] Snarski, S. R., and Lueptow, R.M., "Wall Pressure and Turbulent Structures in a Turbulent Boundary Layer on a Cylinder in Axial Flow," Submitted to J. Fluid Mech., 1994.

[6] Morrison, J. F., Tsai, H.M., Bradshaw, P., "Conditional-sampling Schemes for Turbulent flow, based on Variable-interval time averaging (VITA) algorithm," Experiments in Fluids, Vol. 7, pp. 173–189, 1989.

[7] Wilczynski, V., *Organized Turbulent Structures and Their Induced Wall Pressure Fluctuations,* PhD Dissertation, The Catholic University of America, 1992.

[8] Daubechies, I., *Ten Lectures on Wavelets,* Society for Industrial and Applied Mathematics, 1992.

[9] Meneveau, C., "Analysis of Turbulence in the Orthonormal Wavelet Representation," J. Fluid Mech. No. 232, pp. 469–520, 1991.

[10] Farge, M. "Wavelet Transform and their Applications to Turbulence," Annu. Rev. Fluid Mech., pp. 395–457, 1992.

[11] Zubair, L., "Studies in turbulence using Wavelets Transformations for Data Compression and Scale Separation," Ph.D. Dissertation, Yale, 1993.

[12] Lewalle, J., "Wavelet Analysis of Experimental Data: Some Methods and Underlying Physics," 25th. AIAA Fluid Dyn. Conf., AIAA 94-2281, June 1994.

[13] Liandrat, J. and Moret-Bailly, F., "The Wavelet Transform: Some Applications to Fluid Dynamics and Turbulence," Eur. J. Mech. B/Fluids, vol. 9, No. 1, pp. 111–119, 1990.

[14] Press H., et. al., *Numerical Recipes in C,* Cambridge Press, 1992.

[15] Wark, C. E. and Nagib, H. M., "Experimental Investigation of Coherent Structures in Turbulent Boundary Layers," J. Fluid Mech., No. 230, pp. 183–200, 1991.

[16] Kaftori, D., *Structures in the Turbulent Boundary Layer and their Interaction with Particles,* PhD Dissertation, University of California, Santa Barbara ,1993.

[17] Kaftori D., et. al., "Funnel-shaped vortical structures in wall turbulence," Phys. Fluids, Vol. 6, No. 9, pp. 3035–3050, 1994.